Proceedings World Geothermal Congress 2020+1
Reykjavik, Iceland, April - October 2021

Multi-dimensional and Geological Interpretation of Resistivity Imaging from Magnetotelluric Data in Kiejo-Mbaka Geothermal Field, SW-Tanzania: 2-D, 3-D MT Inversions and Comparisons.

Tumbu L. Boniface and Ngereja M. Mgejwa.

lucas.tumbu98@gmail.com,

nmmgejwa@yahoo.com

Keywords: Multi-dimensional and Geological interpretation, MT 2-D and 3-D inversions, Kiejo-Mbaka geothermal field.

ABSTRACT

This study is aiming at becoming acquainted with the resistivity method and different ways of performing multi-dimensional interpretation of magnetotellurics (MT) data for deep lying subsurface investigations. The aim of modelling magnetotellurics data using the two interpretational techniques is to compare results and establish which resistivity anomalies stand out irrespective of the dimensional inversion used. In this study results from 2-D and 3-D inversions are modelled and compared. The 3-D inversion however, reveals much more consistent details than the 2-D inversions, confirming that the resistivity structures in the area is highly three-dimensional. The resistivity models resulting from the inversion were elevation corrected and smoothed and are presented as planar maps and cross sections.

The real earth is a 3D structure, therefore, 1-D or 2-D may not reliably represent the true subsurface resistivity distributions, for that reason, 3-D inversion is necessary and the comparison of the two inversions techniques, give insights for the true representations of the subsurface structures. The comparison is important as it avoids specifying whether 1-D/2-D or 3-D MT inversion alone as a sole MT imaging approach for deep lying subsurface resistivity structure, 1-D inversion is used as a quality check on 3-D inversion, if no 3-D inversion then 2-D inversion should be requested in daily data robustness testing. The MT dataset collected from Kiejo-Mbaka geothermal area were used, the comparison between the results of 2-D and 3-D inversions with geological information like temperature alteration maps was performed to reconstruct the subsurface resistivity distribution within the study area. Moreover, the MT dataset seems to be highly affected by 3D effects, therefore, 3-D inversion might be more reliable to know the deep structures in the study area. The 2-D MT Occam inversion algorithm was used for 2-D modelling, the results are shown in 2-D sections and depth slices. Notice that their interpretation strongly suffers from 3D effects. 3-D MT inversion using the finite difference (FD) ModEM program was performed. The final model from (Tz+Z) presented here has been obtained from the prior model of tipper (Tz) only, for the whole datasets of 76 sites. The obtained model from (Tz) inversion was carried out using a 100 Ωm half-space as prior model. The inversion runs produced models with a resistive central body surrounded by conductive regions.

The resistive body seems to dip toward SE and is delimited by two surfaces; one dipping toward SW direction with a high angle, another dipping toward NE direction, and less inclined. The first probably, is associated with the Mbaka fault, while the latter has a direction corresponding to the Livingstone fault system. The weak inclination of the second one suggests that it could be interpreted as the top surface of a tilted block, as hypothesized in several geological studies in the area.

Four alteration zones have been inferred from different resistivity iso-surface, three conductive alteration zones inferred from the 10 Ωm iso-surface, and can be referred as low-T alteration zones. Two of them affect in the Mbaka fault foot wall, in the ridge eastern side of the Mbaka escarpment, another low-T alteration zone is located beneath the river plain SE of the Mbaka escarpment. A fourth alteration zone has been identified from the 50 Ωm iso-surface, probably correlated with a N-S fault passing near Lufundo manifestations; this zone could be related to high-T alteration. The assumption that, all the alteration zones should have affected the metamorphic basement has to be considered as per the available geological map.

1. INTRODUCTION

The magnetotellurics method has had an outstanding improvement since its initiation in the 1950s both regarding development of the methodology as well as the capacity of the method to resolve different geological structures. The MT method is the main branch of EM techniques, introduced by (Tikhonov et al., 1950) and (Cagniard et al., 1953). Electromagnetic (EM) theory originates from the four fundamental equations proposed by James Clerk Maxwell. Up to today, the MT technique is still the most powerful method for investigating the deeper lying structure in the subsurface and for describing the resistivity distribution within the area of interest. The measured apparent resistivity is inverted to the actual subsurface resistivity structure by applying multi-dimensional modelling. The geological meaning comes around to support the interpretation. The method has been successful in exploration of geothermal resources in different fields.

This study presents interesting results on the Kiejo-Mbaka geothermal area by use of 76 MT soundings, 2-D and 3-D inversion being interpreted with temperature alteration maps for the study area.

2. THE GEOLOGICAL SETTING OF KIEJO-MBAKA GEOTHERMAL AREA AND GEOTHERMAL MANIFESTATIONS

2.1 Regional Geological Setting

The Kiejo-Mbaka prospect is located within the Rungwe Volcanic Province (RVP) (Figure 1), which is part of the East Africa Rift System (EARS) and covers an area of approximately 1,500 km^2. The Rungwe Volcanic Province (RVP) is situated close to the triple junction of the Rukwa (or Ubende) with NW-SE strike, Usangu (or Usagara) with NE-SW strike and Karonga (or Nyasa) with N-S

strike basins. The northernmost sector of the Karonga basin maintains the NW-SE direction of the Rukwa basin, being delimited to the NE by the NW-SE-trending Livingstone master fault, and is therefore called Livingstone sub-basin.

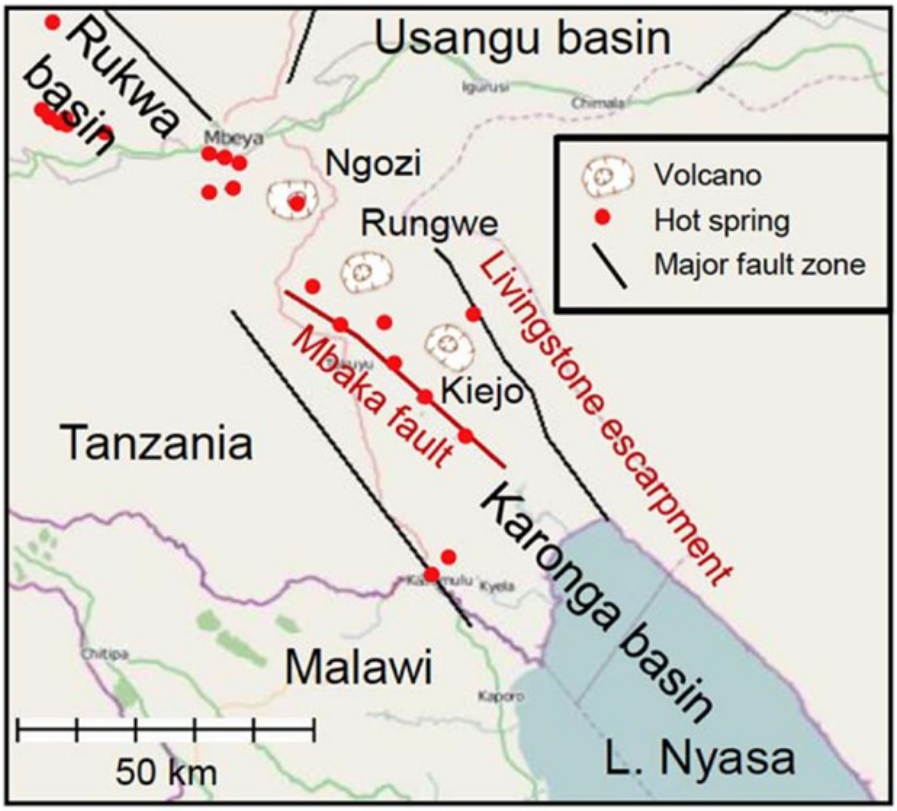

Figure 1: Major geological elements of the study area (from Kraml et al., 2012).

2.2 Local Structural Setting

The structural setting of the study area has been reconstructed through a combination of the observations made in the course of the geological survey by ELC and TGDC (2016) and the results of the remote sensing study, the main results of the remote sensing study have been represented in the form of rose diagrams, which single out the main trends relevant to faults, major fractures, secondary fractures and lineations, as well as to the total field in Figure 2, while Figure 4, shows geological map and the SW-NE geological section namely AA' across the study area from ELC and TGDC (2016), modified and redrawn from (Tumbu, 2019).

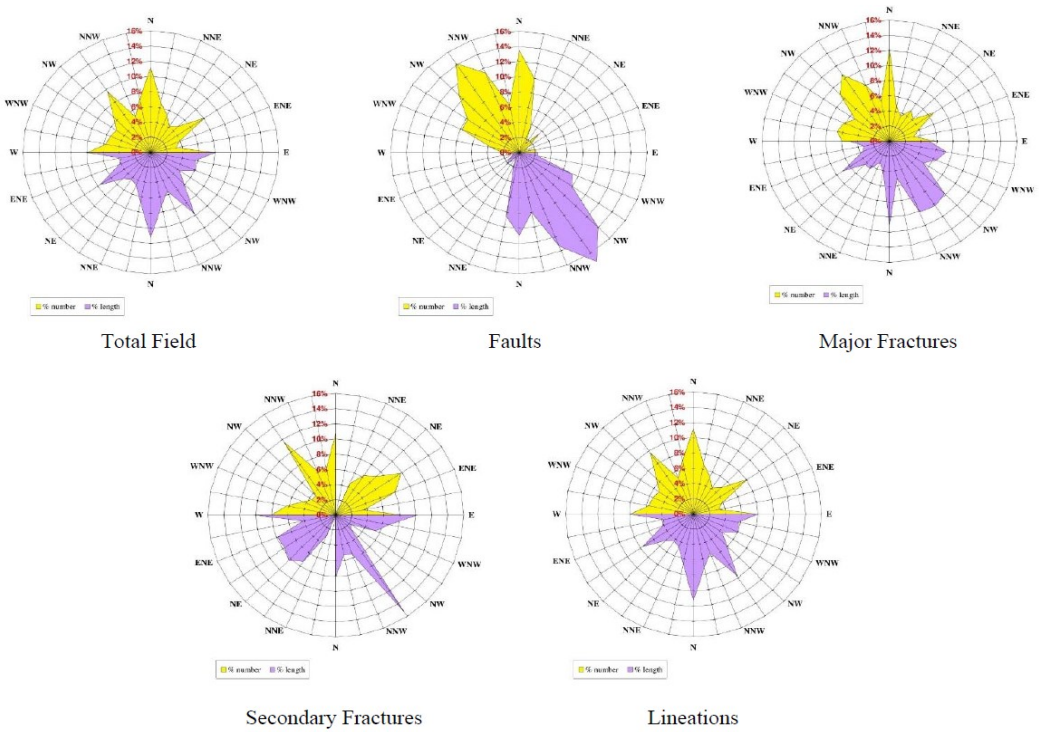

Figure 2: Rose diagrams of linear features according to geological mapping by ELC and TGDC (2016).

2.3 Geothermal manifestations in Kiejo-Mbaka area

Hot springs of Kilambo and gas manifestation of Lufundo; They are found at elevation of about 610 to 665 m a.s.l and 910 m a.s.l respectively, the former is along the Mbaka fault at the intersection with N-S trending structures, extending over a length of 200 m at Kilambo manifestation (Figure 3). The latter is located on the up thrown block to the NE of the Mbaka fault (Mbaka ridge) and is characterized by the natural emission of CO2 rich gases, lack of vegetation and hydrothermal alteration (clay minerals, chlorite and silica). Gas emissions are controlled by N-S and NNW-SSE trending fractures linking two separate steps of the Mbaka fault. The total water flow and maximum temperature at Kilambo is of order of 10 l/s and 64 °C respectively. Thermal waters deposit abundant travertine and Fe(III) oxy-hydroxides and exhibit strong gas emissions.

Figure 3: Kilambo hot spring as one of geothermal manifestations found within the research area.

3. TWO-DIMENSIONAL OCCAM INVERSION

In a 2-D Earth, the coordinate axes are rotated until one of them is along strike, e.g. y is along the strike and x is perpendicular to the strike. As in the 1-D, the diagonal terms (Z_{xx} and Z_{yy}) of the impedance tensor are still zero. The non-diagonal terms (Z_{xy} and Z_{yx}) are not zero, and in general are now unequal. The TE-mode (Transverse Electric) describes the case for which the electric field (E_x) is parallel to the strike, and the magnetic field (H_y and H_z) is perpendicular to the strike.

The TM-mode (Transverse Magnetic) describes the case for which the magnetic field (H_x) is parallel to the strike, and the electric field (E_y and E_z) is perpendicular. For both TM and TE pseudo section models showed reasonable fit with the observed differences between their models and residuals (Figure 5).

2-D inversion has been the standard technique for MT data interpretation in the past decade. It has provided detailed resistivity models in many geothermal fields and has contributed to understanding the resistivity features of geothermal reservoirs. However, because of complicated geological environments which we often encounter in geothermal fields, and the fact, that the real earth is a 3D structure, therefore, 2-D interpretation sometimes has limitations and needs several assumptions, hence fails to produce realistic models.

TE-mode data are excellent and more sensitive for isolating a deeper conductive anomaly in a 2-D situation than TM-mode data does for isolating deeper resistive anomaly. However, unless the subsurface structure is almost 2-D, we usually cannot achieve a good fit for TE-mode data by a 2-D inversion. On the other hand, fitting of TM-mode data in a 2-D inversion can be more easily achieved even for a 3-D structure, especially when the profile crosses the 3-D structure at the center. This is why we often utilize only TM-mode data for 2-D inversion in geothermal exploration.

Even if the misfit of the TM-mode data is small, the recovered 2-D model may be unrealistic or contain false anomalies. This is the reason why one may prefer a TE-mode jointly with TM-mode as applied in this research. In particular, the subsurface resistivity distribution in deeper parts of the reservoir is often ambiguous. This situation illustrates the limitations of the 2-D MT interpretation in geothermal exploration Uchinda and Sasaki (2006).

For 2-D inversion of Kiejo-Mbaka MT data, we used the Occam's 2-D inversion code. Occam's 2-D inversion is based on the minimization of the following unconstrained functional;

$$U = \left\|\partial_y \boldsymbol{m}\right\|^2 + \|\partial_z \boldsymbol{m}\|^2 + \mu^{-1}\{\boldsymbol{W}\|\boldsymbol{d} - \boldsymbol{F}(\boldsymbol{m})\|^2 - X_*^2\} \quad (1)$$

where the expression, $\left\|\partial_y \boldsymbol{m}\right\|^2 + \|\partial_z \boldsymbol{m}\|^2$ is a norm of the model roughness, μ^{-1} is the Lagrange multiplier, the third term in the equation represent the data misfit, $\boldsymbol{W}$ **is** $M \times M$ diagonal weighting matrix, $\boldsymbol{d}$ represents the observation vector and $\boldsymbol{F}(\boldsymbol{m})$ stands for the model response.

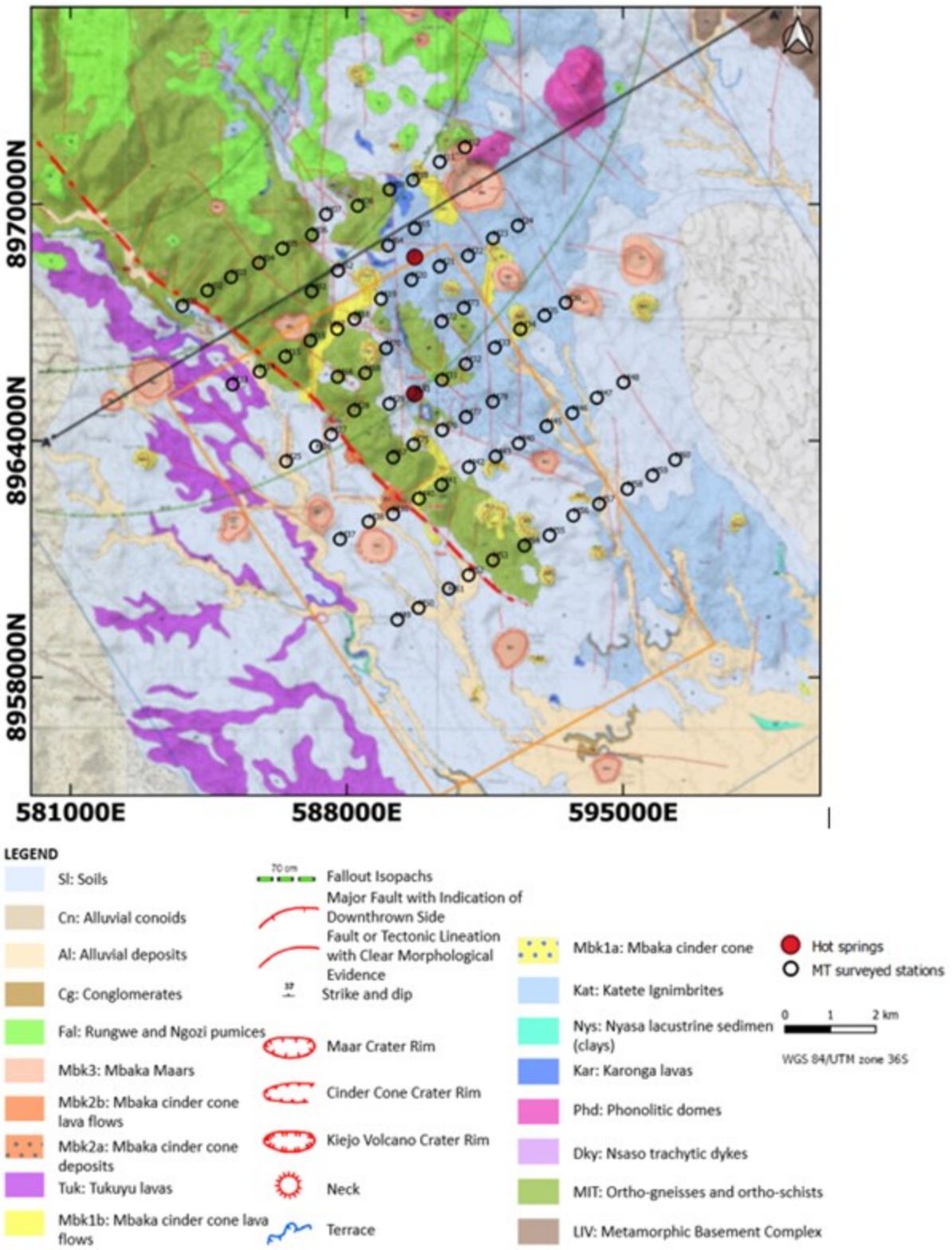

FIGURE 4: Geological map of the study area. AA': trace of the geological section by ELC and TGDC (2016), modified and redrawn from (Tumbu, 2019). Red rectangle: MT survey area. Lithologies are briefly described in the text. Red dotted line indicates the Mbaka fault escarpment.

3.1 2-D Resistivity Models Recovered from 2-D Occam inversion

The profiles have been divided into two groups, with different orientation: **WSW-ENE** (profile lines KML1, KML3 and KML5) and **NNW-SSE** (profile lines KML9 and KML11) in Figure 6. The resulting resistivity models are shown in Figures 7 and Figure 8.

Interpretation of Occam's 2-D inversion results have shown the most remarkable features as following:

3.1.1 Transversal sections:

(1) The sections are characterized by a central resistive core "**R**" resembling with the Precambrian Intrusive Metamorphic basement complex marked as "**MIT**" in the geological map (see Figure 4). The high resistivity values it reaches may be as a consequence of the extreme 3D effects observed in the area; (2) **C1** is a thick and quite continuous conductor beneath the rift basin westward of the Mbaka fault; this layer shows locally very low resistivity values <1 Ωm. According to the known geology, this thick conductor should be described to a wide low-T alteration zone in the Precambrian basement. Its plausible also may include some fluvio-lacustrine Neogene sediments in the rift basin; (3) **C2** is thin and could be related to a shallow low-T alteration zone in the LIV gneiss. Its minimum resistivity is <5 Ωm; (4) **C3** is deeper and discontinuous; it could be related to a deeper low-T alteration zone in the LIV gneiss. The minimum resistivity is <10 Ωm; (5) the discontinuity **D1** is in good agreement when correlated with the Mbaka fault and marks a border between the conductive layer in the river plain (**C1**) and the resistive rift shoulder (**R**) constituted by the LIV gneiss; (6) the discontinuity **D2** marks a border between the resistive zone "**R**" and the more conductive zone toward east comprising **C2** and **C3**.

3.1.2 Longitudinal sections:

(1) **C1** is thick and continuous; (2) **C2** is shallow and continuous; toward south (profile line KML8) it merges with the conductive layer **C1**; (3) on the eastern side of study area (along profile line KML11), **C3** is not continuous and is poorly extended; and the resistive zone **R** is marginally perceived; (4) one discontinuity transversal to the Mbaka fault may be hypothesized as (**D3?**).

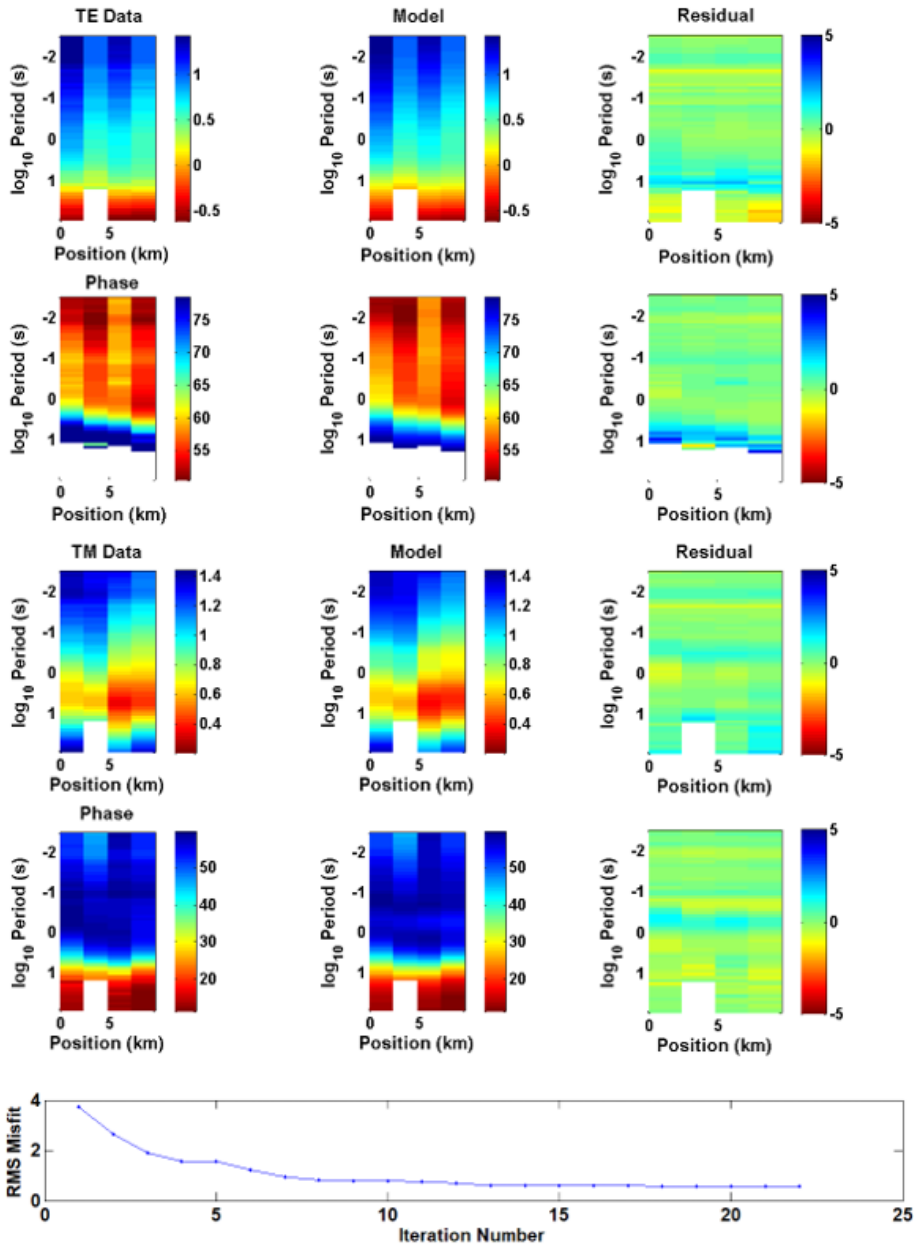

Figure 5: Top: TE and TM resistivity pseudo sections showing the differences between data and the models with residuals approximately zero, as an indication of a reasonable fit. Bottom: is a transition curves of R.M.S error with the iterations.

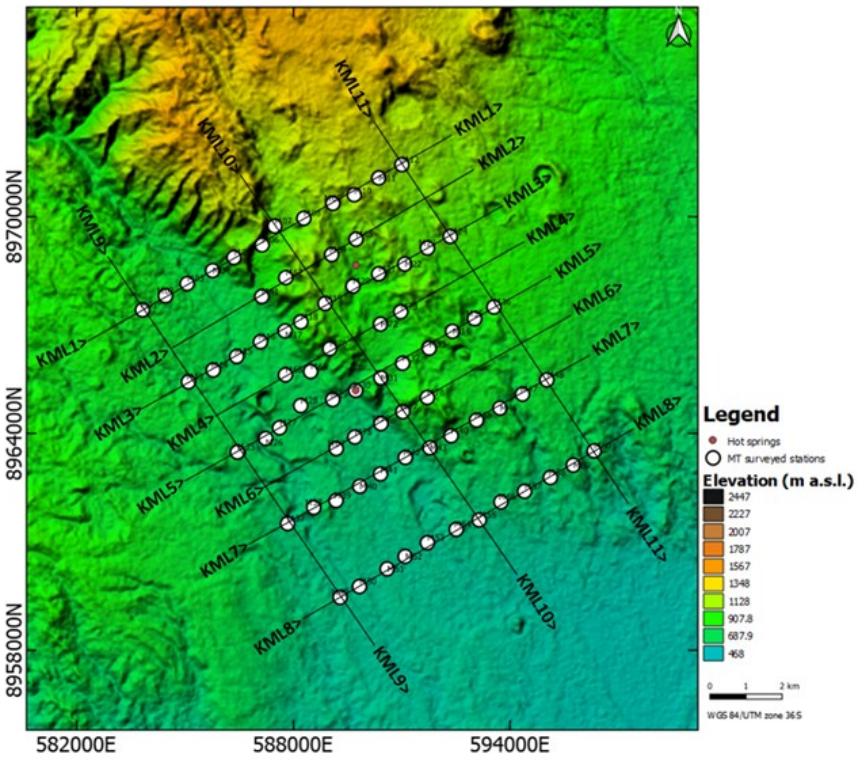

Figure 6: Location map for MT sites. The (> <) symbols indicate the orientation of the corresponding profile lines. White circles mark the MT sites. Red dots indicate the Kilambo hot springs and Lufundo manifestations.

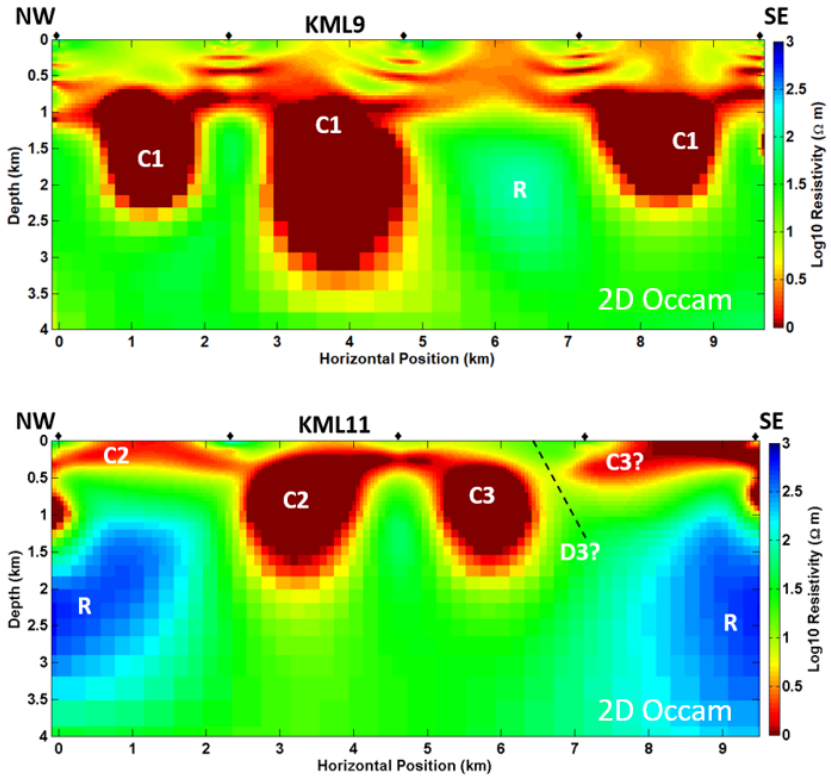

Figure 7: NNW-SSE trending profile lines KML9 and KML11.

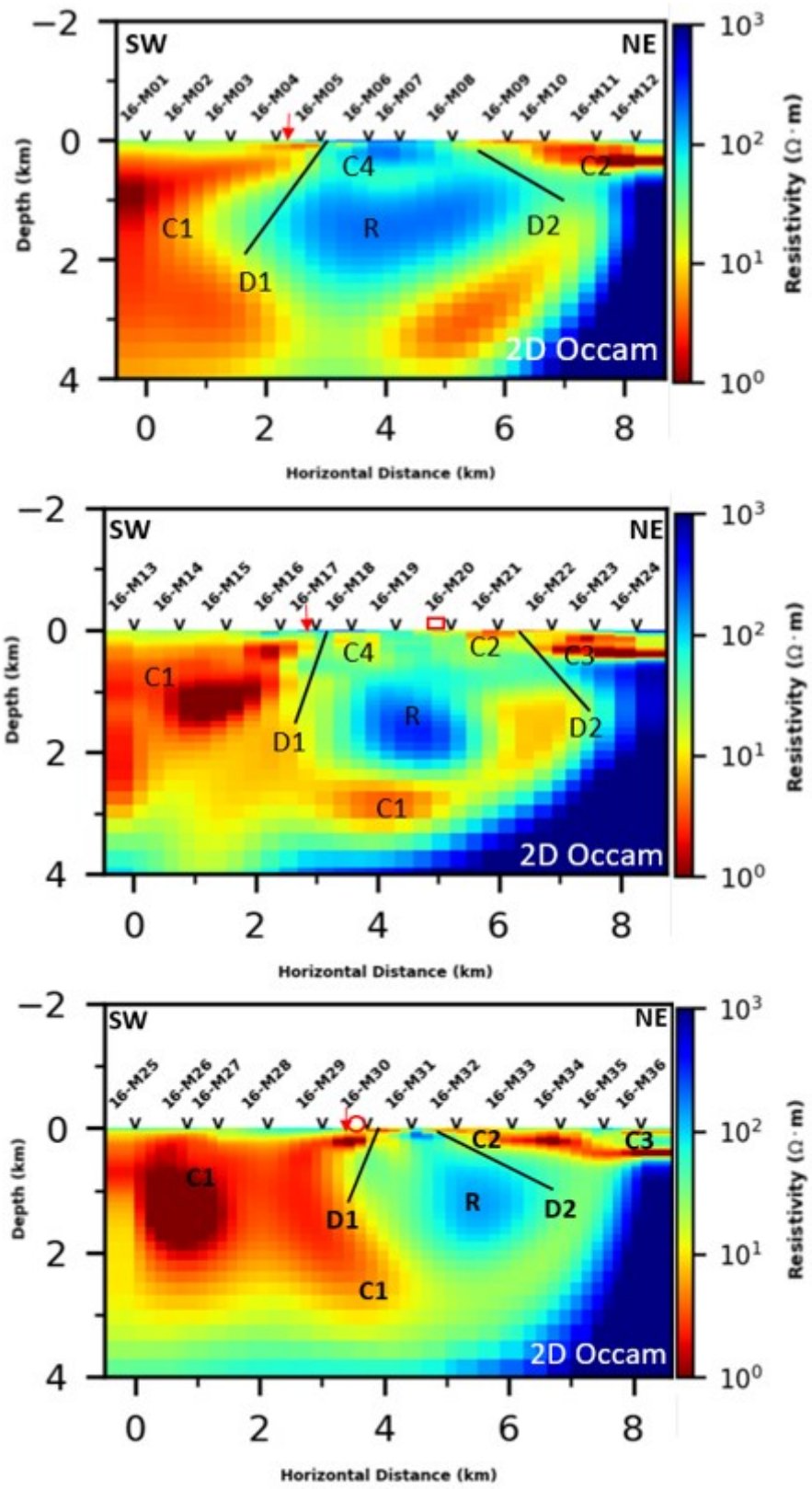

Figure 8: WSW-ENE trending profile lines KML1, KML3 and KML5. The Mbaka fault is marked by red arrow, while Kilambo hot spring is shown by red circle.

4. THREE-DIMENSIONAL OCCAM INVERSION

4.1 3-D ModEM Inversion

For 3-D inversion we used the ModEM software of (Kelbert et al., 2014) with additions for parallel computing described by (Meqbel et al., 2009). ModEM is based on a finite differences (FD) approach to solve Maxwell's equations on a staggered grid, and inversion is performed by minimization of the following functional:

$$\boldsymbol{\Phi} = (f(\boldsymbol{m}) - \boldsymbol{d})^T \boldsymbol{C}_d^{-1} (f(\boldsymbol{m}) - \boldsymbol{d}) + \lambda(\boldsymbol{m} - \boldsymbol{m}_0)^T \boldsymbol{C}_m^{-1} (\boldsymbol{m} - \boldsymbol{m}_0) \quad (2)$$

where *f(m)* is the FD nonlinear forward operator that maps the model vector *m* from the model space into the data vector *d* in the data space, *m* is the conductivity model, m_0 is the priori conductivity model, *d* is the observed data vector, C_d is the data covariance matrix, C_m is the model covariance matrix, λ is a trade-off parameter between data fit and regularization.

For the 3-D inversion results presented in this paper, the functional Φ has been minimized by the Non-Linear Conjugate Gradient (NLCG) scheme e.g. Rodi and Mackie (2001); (Kelbert et al., 2014). From the above functional, it can be deduced that the inversion scheme penalizes model perturbations obtained after each iteration against a prior model. we stress that in ModEM the starting and prior model are coincident.

The model grid used for the dataset under consideration consists of 37 x 38 x 60 cells in x, y, and z directions (84,360 cells in total). In the central portion (core) of the model, the dimensions of the boundary blocks increased with a factor of 2 in both x and y directions while the z direction increased by factor of 1, the vertical direction with 55 layers were used in the model. The thickness of the first layer was set to 10 m and the subsequent layers increase by a factor of 2 as shown in Figure 9, the MT sites location up to a depth of about 8 km are also shown in the same figure, as it can be observed, topography has been taken into account by model discretization and the vertical spacing also increases logarithmically above the topography surface. Figure 10, shows the 3-D model grid, constructed from 3-D inversion using ModEM program and the detailed vertical grid used along an EW transect in the central part of the grid with a maximum depth up to 8 km.

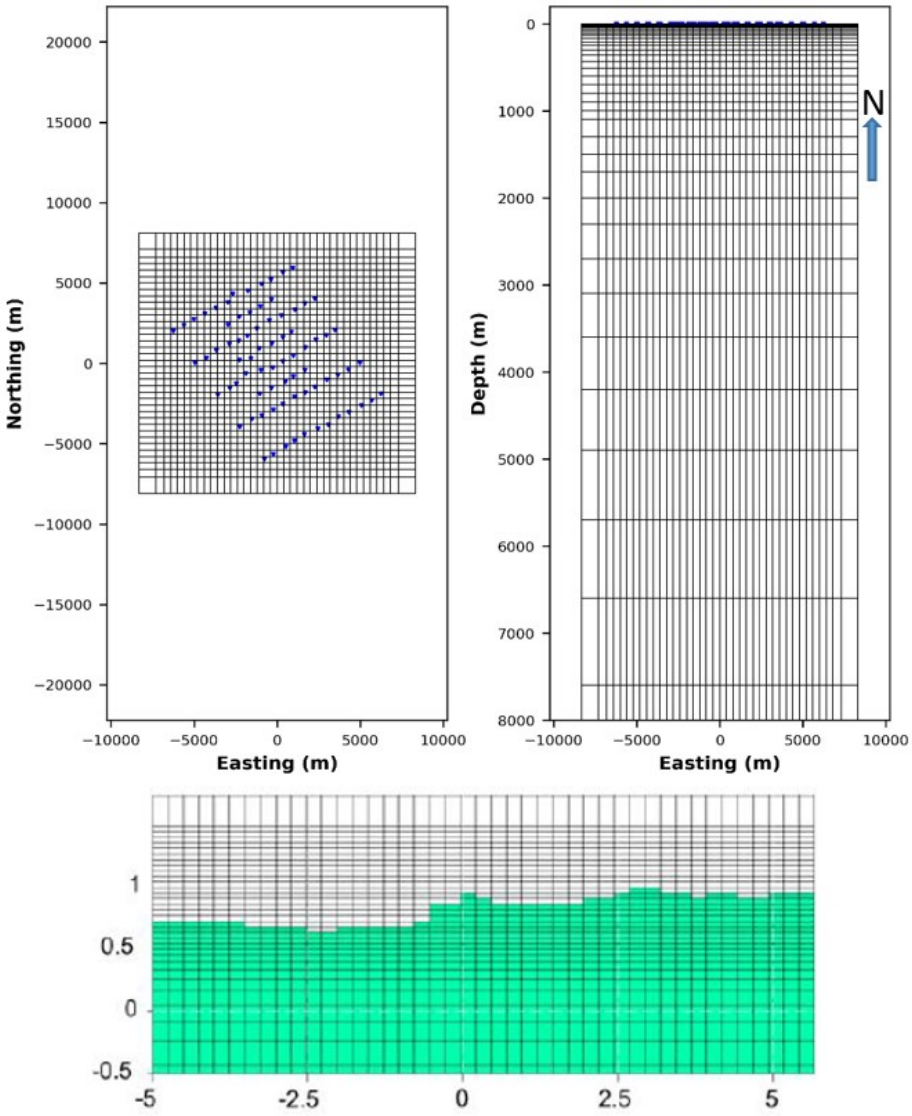

Figure 9: Central part of the horizontal grid used. Site locations are marked by blue dots. In the vertical (z) direction, the grid consists of 55 layers and then the grid spacing augments logarithmically with depth, a detailed view of the central part of the grid, up to a depth of about 8,000 m. maximum depth: 8,000 m. Topography has been taken into account by model discretization and the vertical spacing also increases logarithmically above the topography surface.

4.1.1 Inversion Settings for 3-D ModEM Program

The final model resulted from (Tz+Z) 3-D inversion presented here, we used the full (unrotated) and static shift - corrected impedance tensor (Z) from the whole dataset of (76 sites), using 85 periods in the range between 0.00128 s-2,941 s. we assigned error floors of 10 % of $\sqrt{|Z_{xy}Z_{yx}|}$ to the Z_{xy} and Z_{yx} impedance tensor components, and 20 % of $\sqrt{|Z_{xx}Z_{yy}|}$ for Z_{xx} and Z_{yy}. Some heavily biased or scattered data points were manually discarded after inspection. A final model obtained from a prior model for the 3-D inversion of the tipper (Tz) data only, was accomplished by using a homogeneous 100 Ωm half-space and assigned a constant value of 0.05 as an error floor.

4.2 Interpretation of 3-D ModEM Inversion Results

This section briefly discusses the results from the inversions of the tipper (Tz) and impedance tensor (Z); the resulting models are displayed by mean of horizontal resistivity depth slices in in Figure 16. It can be observed that the models show the general features, namely a resistive central body and conductive regions around it. These features will be explained later in details for the interpretation part of this paper.

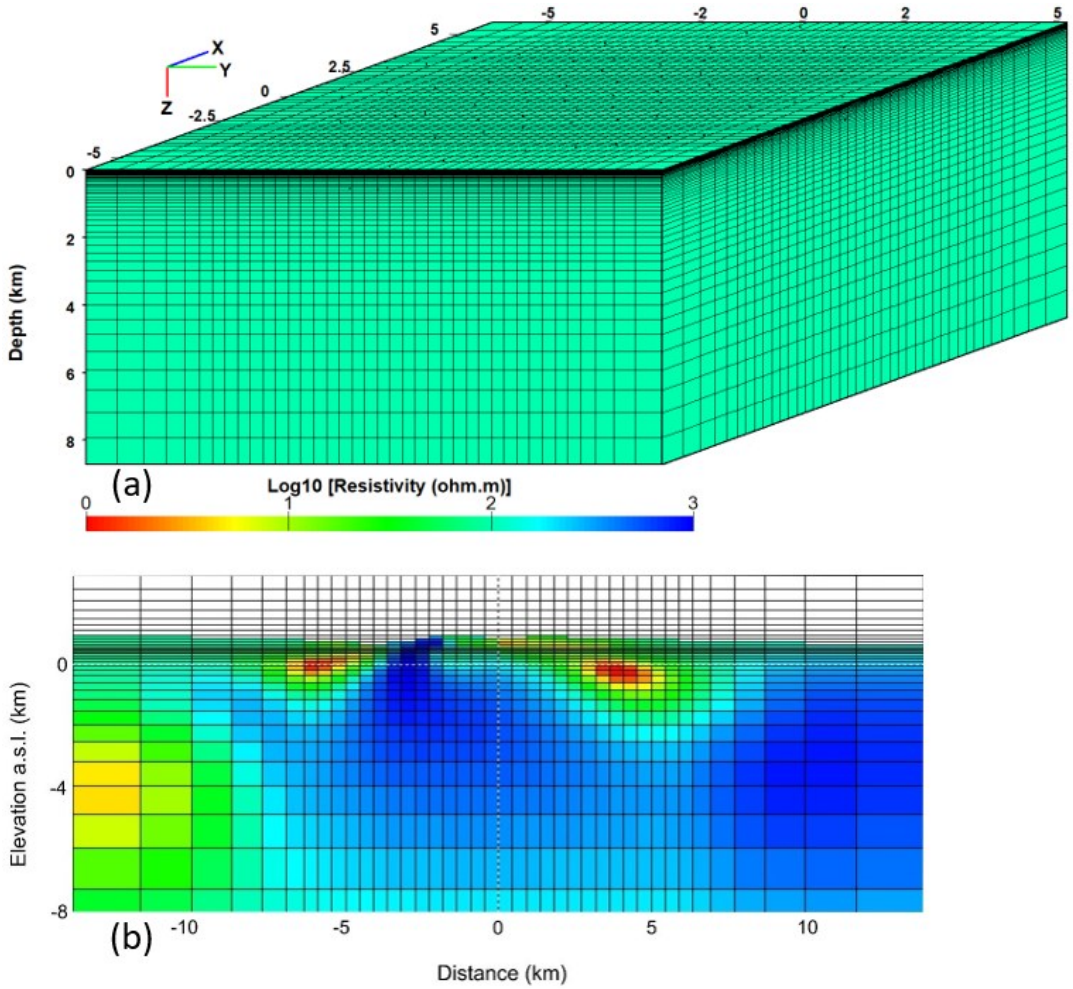

FIGURE 10: (a) 3D model grid, constructed from 3-D inversion using ModEM program; (b) Detailed vertical grid used along an EW transect in the central part of the grid. Maximum depth: 8 km. Vertical exaggeration: 1.

4.2.1 Resistivity Cross-sections and Horizontal Depth Slices

The 3-D model is presented hereinafter by means of resistivity cross-sections along the profile lines and with horizontal resistivity depth slices maps as shown in Figure 6 for the MT site locations. The **WSW-ENE** sections KML1, KML3 and KML5 are shown in Figures 14 and the **NNW-SSE** sections KML9 and KML11 in Figure 15, whereas Figure 16 shows the horizontal depth slices map.

The general features that can be identified are similar to those discussed in (2-D modelling) section, However, the 3-D inversion allowed much better to understand the geometry of such features, as noticed in the following models, the features are relatively better resolved at greater depth as compared to 2-D results, bearing in mind that the area of research is strongly affected by 3D effect, therefore, 3-D inversion results may be more realistic than 2-D results. Though the lithology in the area is mostly dominated by the Intrusive Metamorphic basement and Gneiss (**MIT** and **LIV**) metamorphic complexes. Therefore, several anomalous resistivity zones have been identified; this leads to infer that resistivity is not directly related to lithologies. The apparent resistivity sounding curves

and phase responses for all 76 MT sites and for selected sites M13 and M45, together with the 3-D resistivity distribution model recovered from MT 3-D inversion using ModEM programs are shown in Figure 11-13.

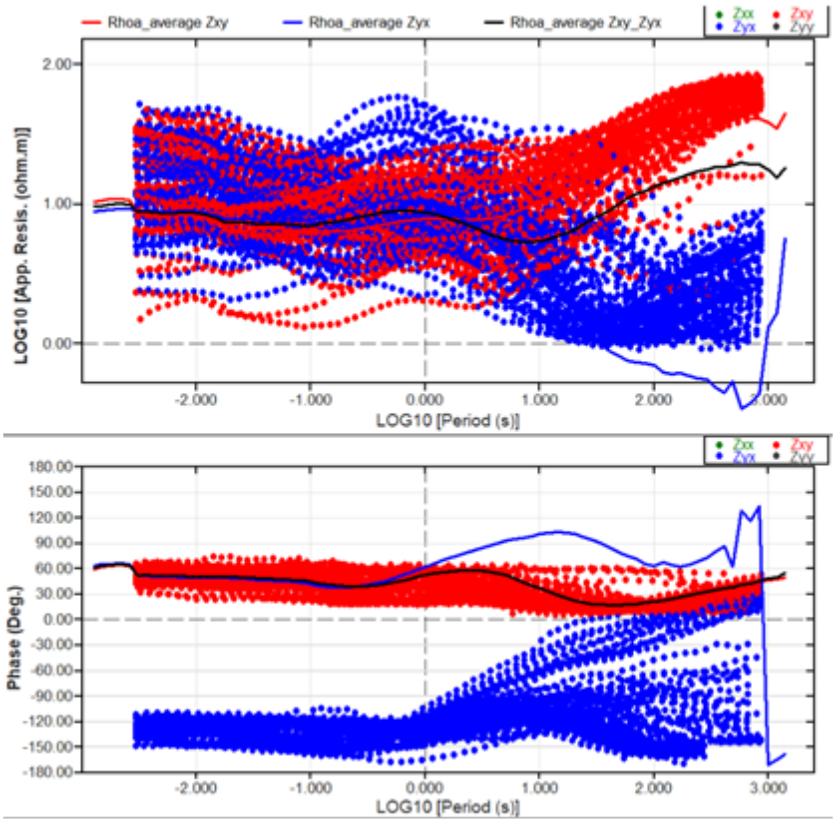

Figure 11: Apparent resistivity sounding curves and phase responses for 76 MT sites recovered from 3-D MT inversion using ModEM programs.

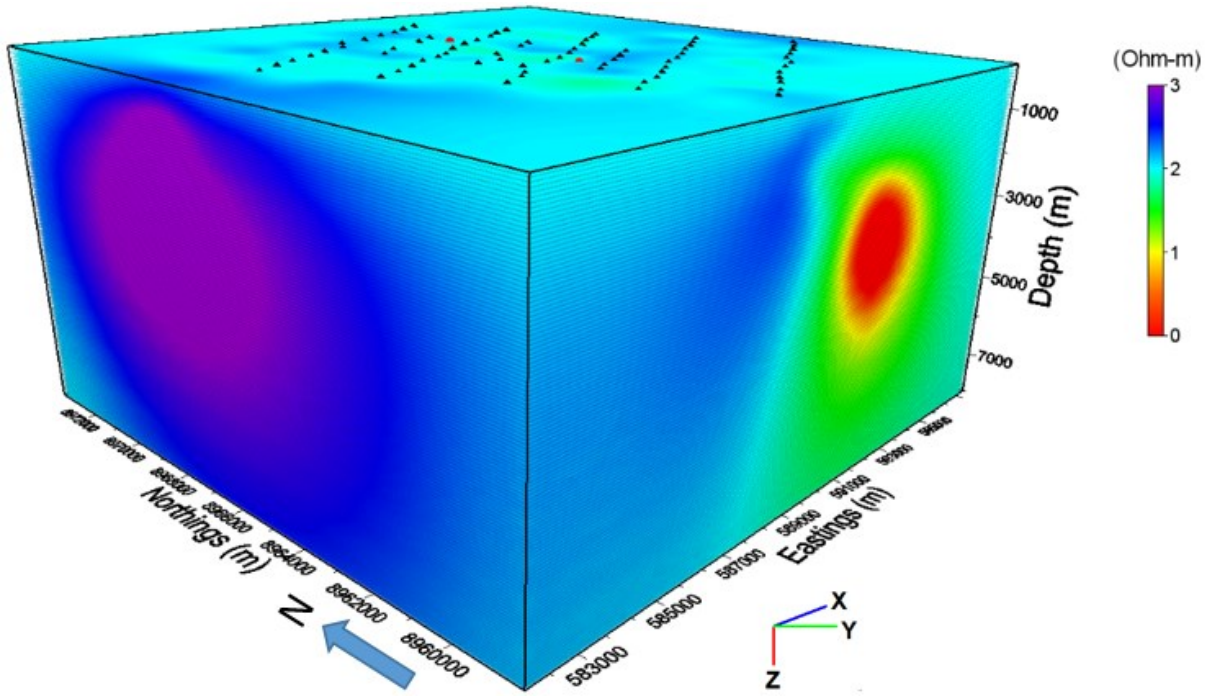

Figure 12: 3-D resistivity distribution of Kiejo-Mbaka geothermal field recovered from 3-D MT inversion using ModEM programs, Kilambo hot spring and Lufundo manifestations are marked by red dots. MT surveyed stations are represented by black dots for reference.

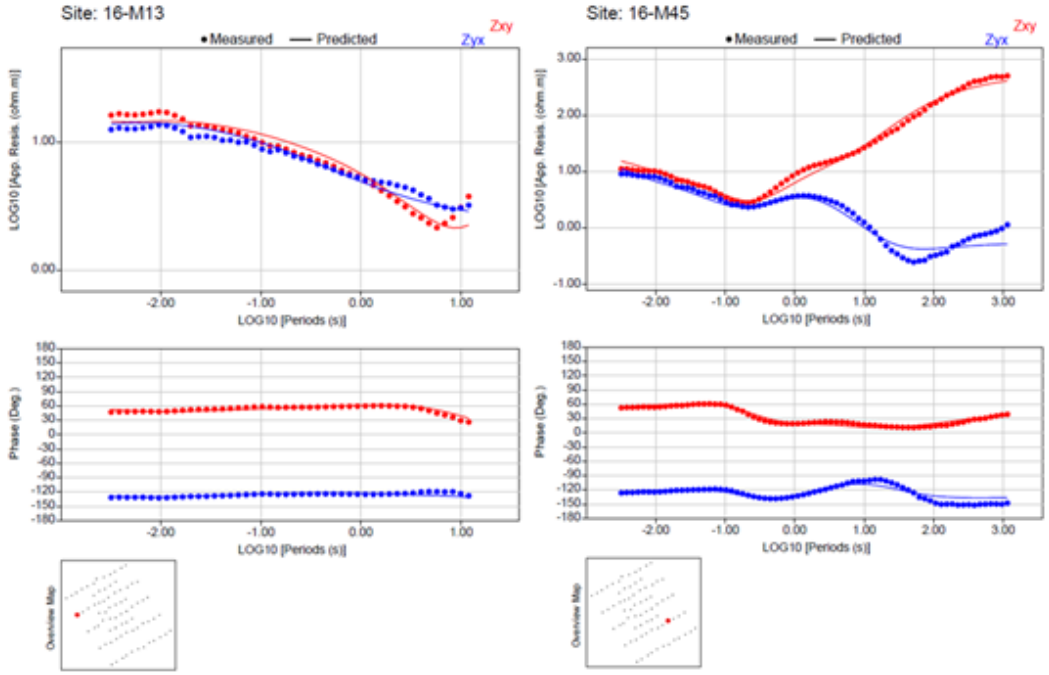

Figure 13: Typical sounding curves, as an example of data fit showing the response for station M13 and M45. Top: xy and yx apparent resistivities; bottom: xy and yx phases response for two sites. The bottom panels indicate site locations.

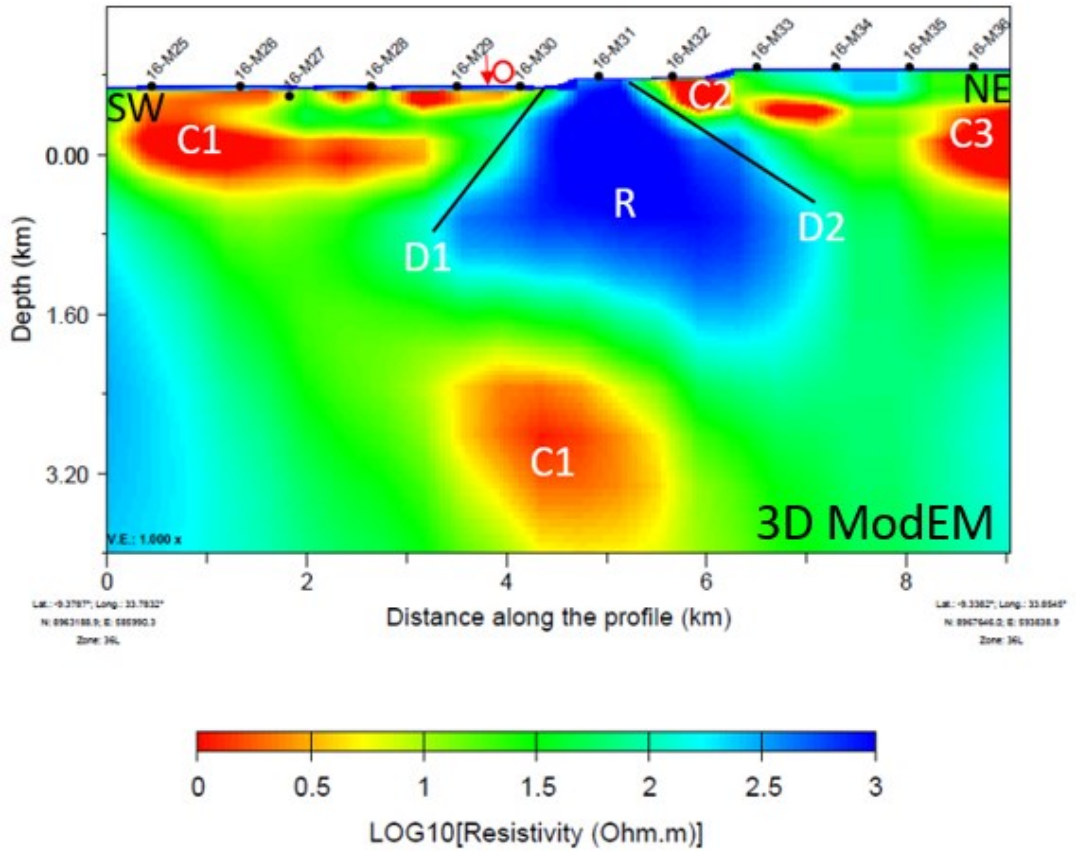

Figure 14: WSW-ENE trending profile lines KML5. The Mbaka fault is marked by red arrow, while the Kilambo hot spring is indicated by red circle.

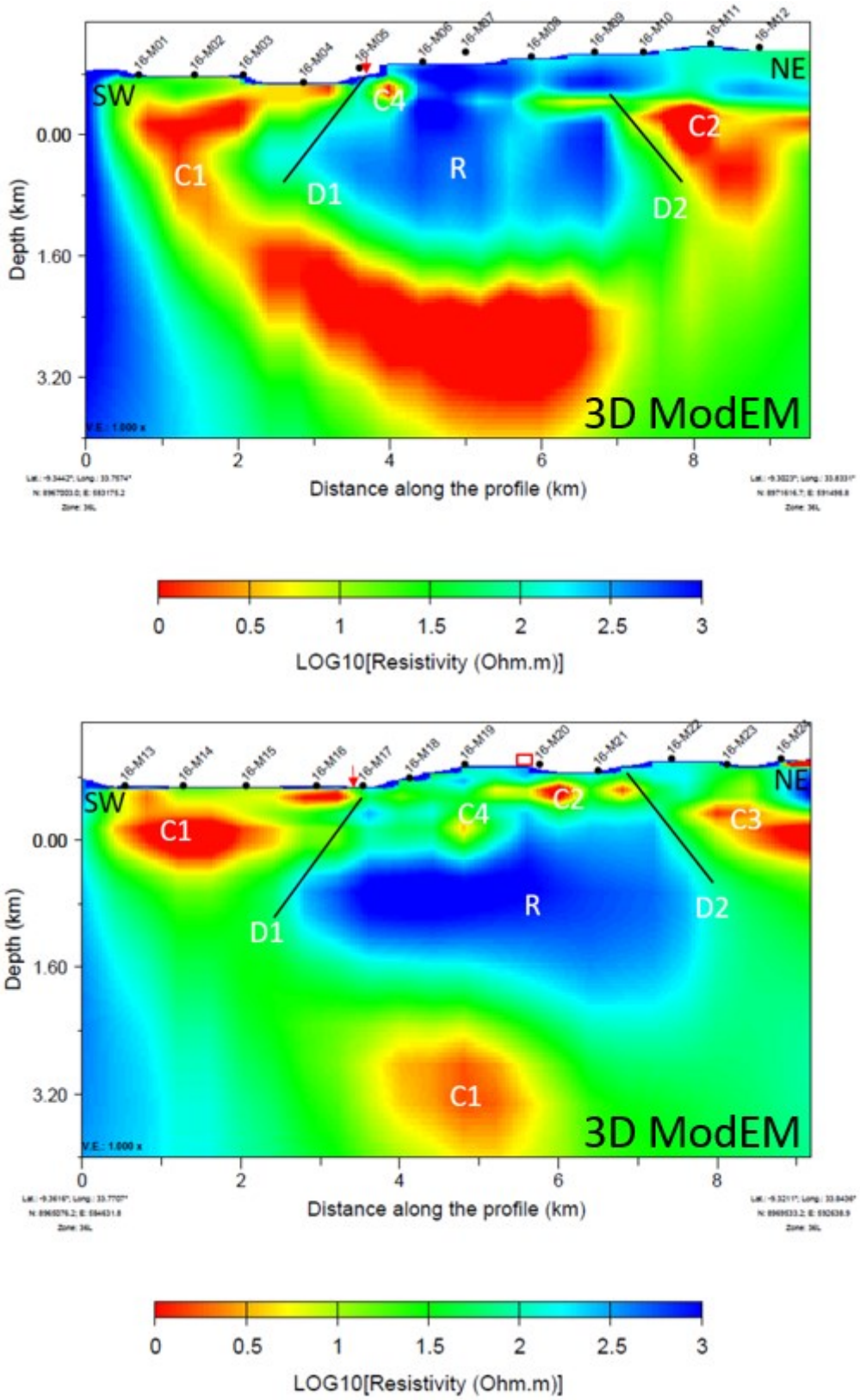

Figure 14: Continued; WSW-ENE trending profile lines KML1 and KML3. The Mbaka fault is marked by red arrow, while the Lufundo manifestation is indicated by red square.

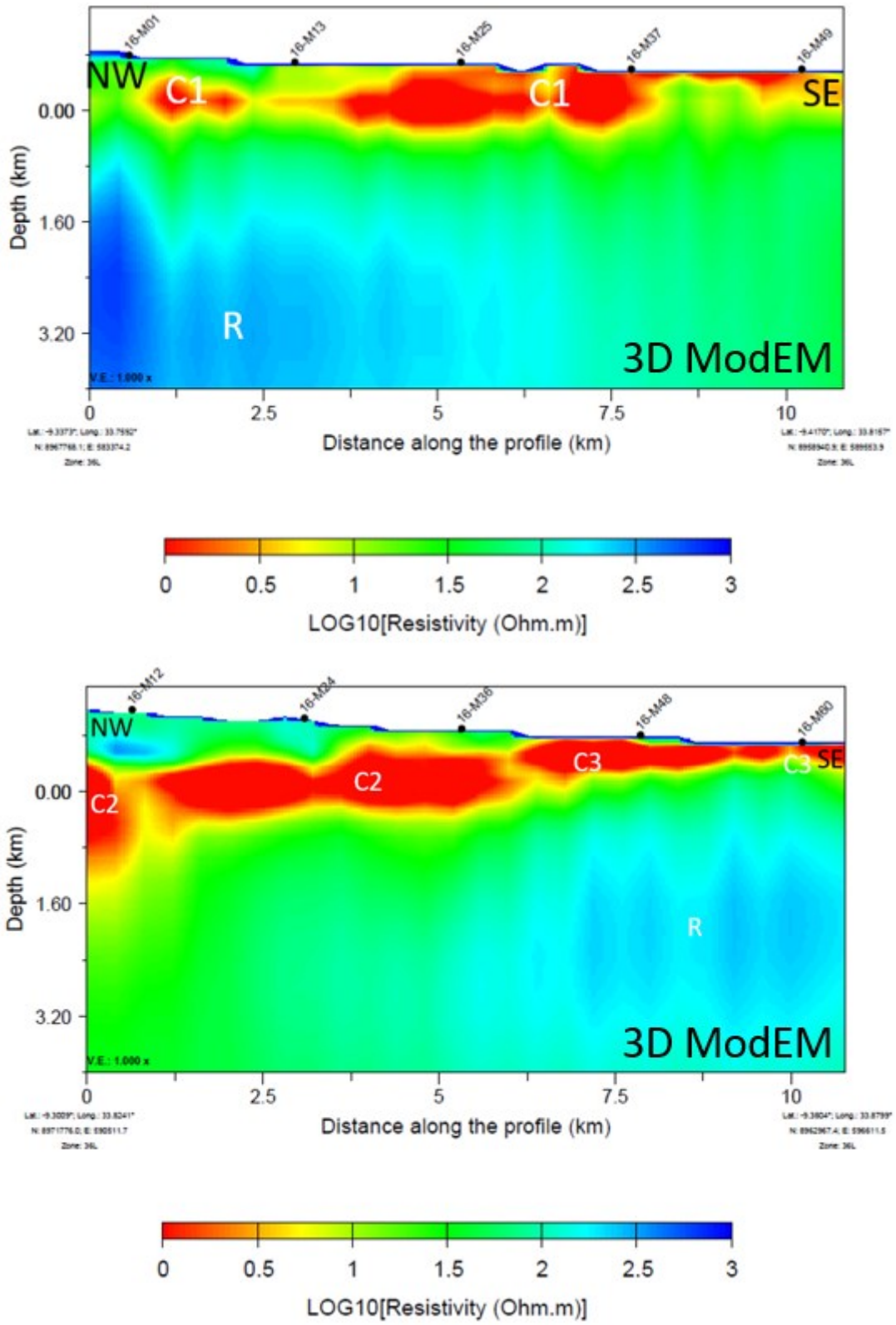

Figure 15: NNW-SSE trending profile lines KML9 and KML11.

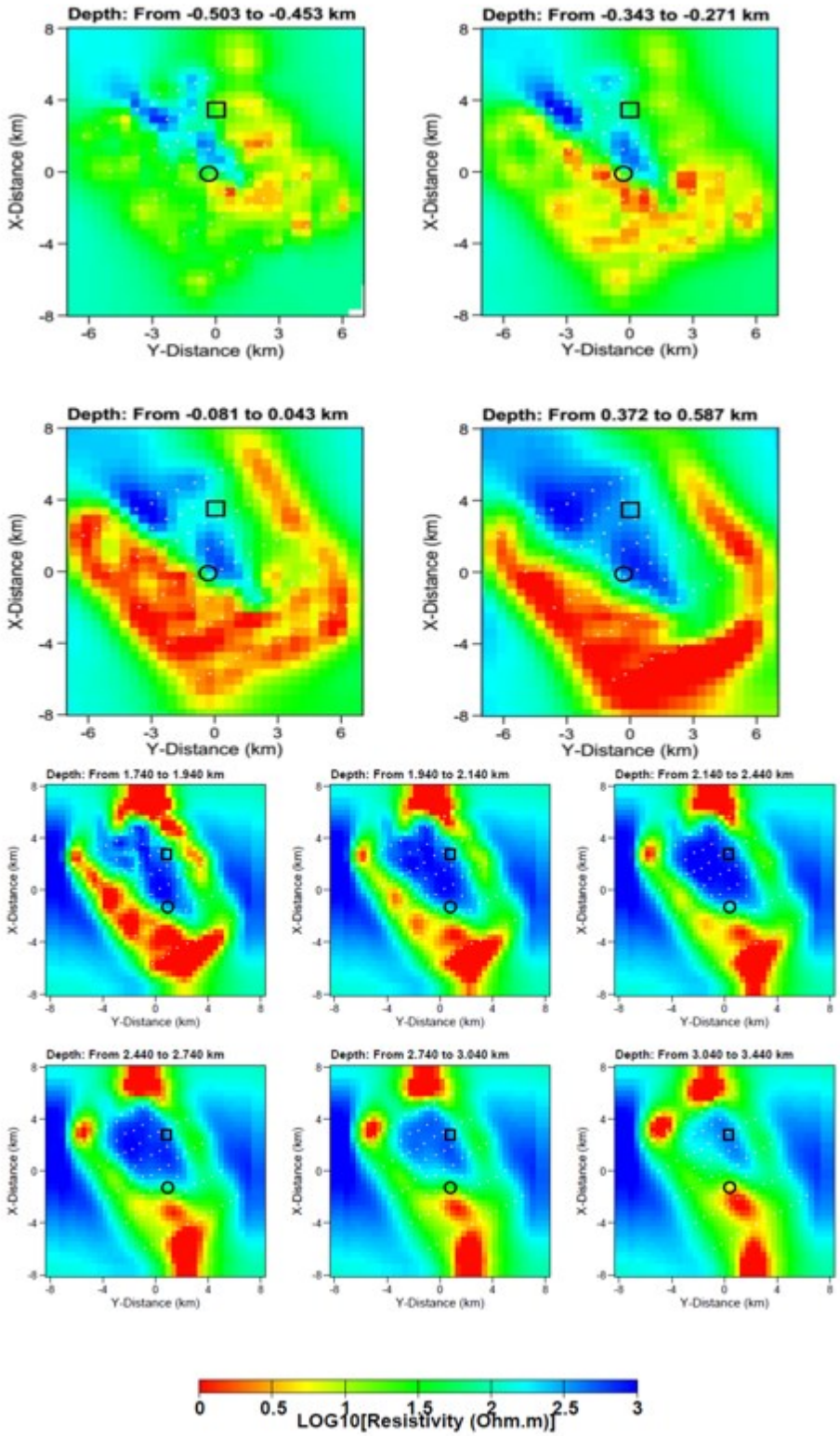

Figure 16: Inversion results for the (Z) from homogeneous 100 Ω m initial model. MT stations grid are marked by white dots. Depths are intended positive downward starting from 0 m a.s.l. The Kilambo hot springs are marked by a black circle, while the Lufundo Manifestations by a black square.

5. COMPARISONS OF 2-D AND 3-D RESISTIVITY MODELS WITH GEOLOGICAL CROSS-SECTION AND TEMPERATURE ALTERATION MAPS

This section compares and contrasts between the results obtain from the inversions using Occam approach schemes for 2-D resistivity models and ModEM program for 3-D resistivity models. The correlation between the inversion results with geological cross section

and temperature alteration maps for the study area is done under this section. The temperature alteration zones identified during geological mapping by ELC and TGDC (2016) is compared with our 2-D and 3-D inversion results.

The main features that can be inferred from the sections and from the slices in both 2-D and 3-D resistivity model are very similar in general and being characterized as follows:

5.1 Transversal Sections:

(1) The sections are characterized by a central resistive core "**R**" corresponding with the outcropping Precambrian Intrusive Metamorphic basement and Livingstone Gneiss respectively marked as "**MIT**" and "**LIV**" in the geological map, see Figure 4; (2) anomaly **C1** is a thick conductor beneath the rift plain westward of the Mbaka fault; this layer shows locally very low resistivity values (< 1 Ωm). According, to the geological map, this conductive feature could be interpreted as a wide low-T alteration zone in the Precambrian basement. Its plausible also may include some fluvio-lacustrine Neogene sediments in the rift basin.

(3) anomaly **C2** is a thin and shallow conductor with minimum resistivity (<5 Ωm), that could be related to a low-T alteration zone in the **MIT** basement. In profile line KML3, this anomaly could be associated with the Lufundo fossil manifestations; (3) anomaly **C3** is a deeper and further to east conductor; given its resistivity as low as (<10 Ωm) it could be related to a low-T alteration zone in the **MIT** and/or in the Livingstone rift (**LIV**) metamorphic rocks.

(4) anomaly **C4** is a relatively resistive zone that affects the **MIT** basement; given its resistivity (<50 Ωm) it could represent a high-T alteration zone; (5) discontinuities **D1** and **D2** have been pinpointed by following the 100 Ωm iso-resistive:

(a) The discontinuity **D1** can be roughly correlated and associated to the Mbaka fault and marks a border between the conductive layer in the river plain (**C1**) and the resistive rift shoulder (**R**) constituted by **MIT** and **LIV** metamorphic rocks. However, in 2-D and 3-D inversion models, it can be noticed that the position of the **D1** discontinuity does not generally match at the surface with the location of the Mbaka fault marked by a red arrow. A quite good agreement in correlation can only be observed in the profile line KML1, where it also has a dip in good agreement with the fault dip reported in (Biggs et al., 2010).

The fact that **D1** does not have a good matching with the Mbaka fault, indicates that the latter one may be does not have a clear resistivity signature, probably not tectonic factors that govern the resistivity distribution. If we assume that the anomaly **C1** has been produced by low-T alteration in the **MIT**/**LIV** basement, it seems that this alteration zone extends toward NE beyond the expected Mbaka fault, which affects also its foot wall.

(b) The discontinuity **D2** marks a border between the resistive rift shoulder (**R**) and the conductive zones toward east **C2** and **C3**.

5.2 Longitudinal Cross Sections:

(1) On the eastern side of the survey area along profile line KML11, it can be seen that **C2** is shallow about 250-450 m and discontinuous and **C3** is also discontinuous but deeper (550-850 m); (2) one discontinuity transversal to the Mbaka fault might be hypothesized as (**D3?**) from profile lines KML11; (5) finally, it can be noticed from all the profile lines seen, that the resistive central 'core' **R** deepens toward SE. However, from 2-D resistivity models in some of the profile lines this fact is not clearly evidenced owing to strong 3D effects.

5.3 Resistive Central Body

(1) The resistive "core" **R** is visible in the central portion of the survey area and is in good agreement with the outcropping Precambrian Intrusive Metamorphic basement (**MIT**) refer to geological map Figure 4. The two sections E-W and N-S Figure 19, speculated the order of resistivity from the surface to deeper portion, are excellently isolated the resistive central core '**R**'. The sections were drawn using **Voxel Software**. The aforementioned resistivity anomalies **C1**, **C2**, **C3**, **C4** and **R**, are reasonably reconstructed as shown in Figure 19. As a matter of fact, software artifacts were tested by reconstructing the same sections by the use of **3-D-Grid-Academic tool**, the results, were almost similar beyond doubts, as can be seen in Figure 20. At the shallowest depths, the aforementioned anomaly **C4** is observable in all the Figures:

(2) the plain area westward of the Mbaka fault shows resistivities of about 100 Ωm at shallow depths; these values are in good agreement with the presence of the shallow Tukuyu Basalts (see Figure 4); (3) the conductive zone **C1** is visible on the western side of the Mbaka fault, this zone has resistivity (<0.5 Ωm); (4) the conductive zone **C2** is visible on the eastern side of the Mbaka fault and has resistivity (<10 Ωm), at the shallowest depths, it seems to be related to the Lufundo manifestations; (5) the conductive zone **C3** is visible on the eastern side of the Mbaka fault and at relatively deeper depths. Its resistivity generally (<20 Ωm). Moreover, it can be noticed that the widening of the resistive core **'R'** at depth reflects the south-westward dip of the Mbaka fault and the north-eastward dip of the discontinuity **D2**, refer to 2-D and 3-D models.

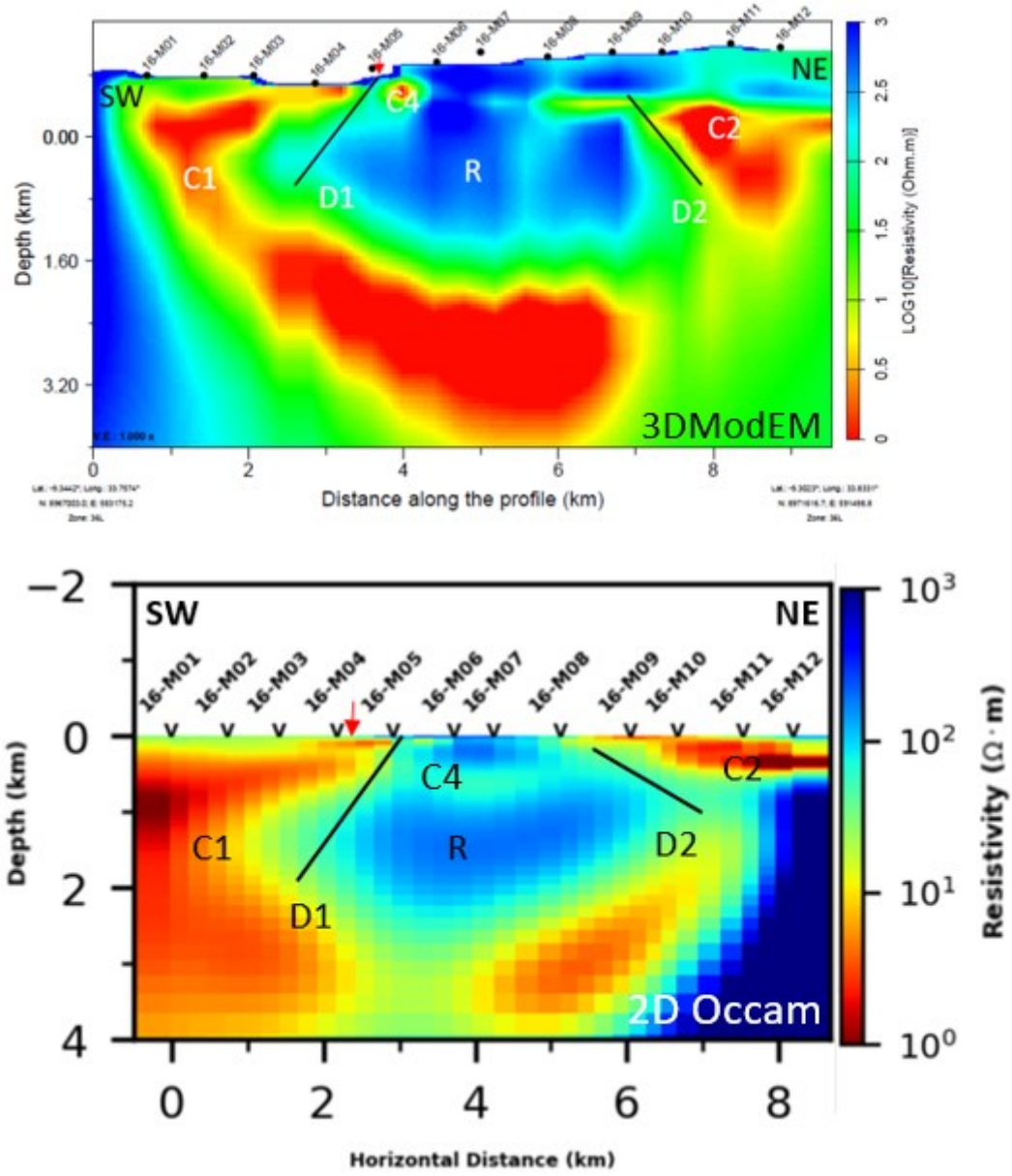

Figure 17: WSW-ENE trending profile line KML1. The Mbaka fault is marked by red arrow for references.

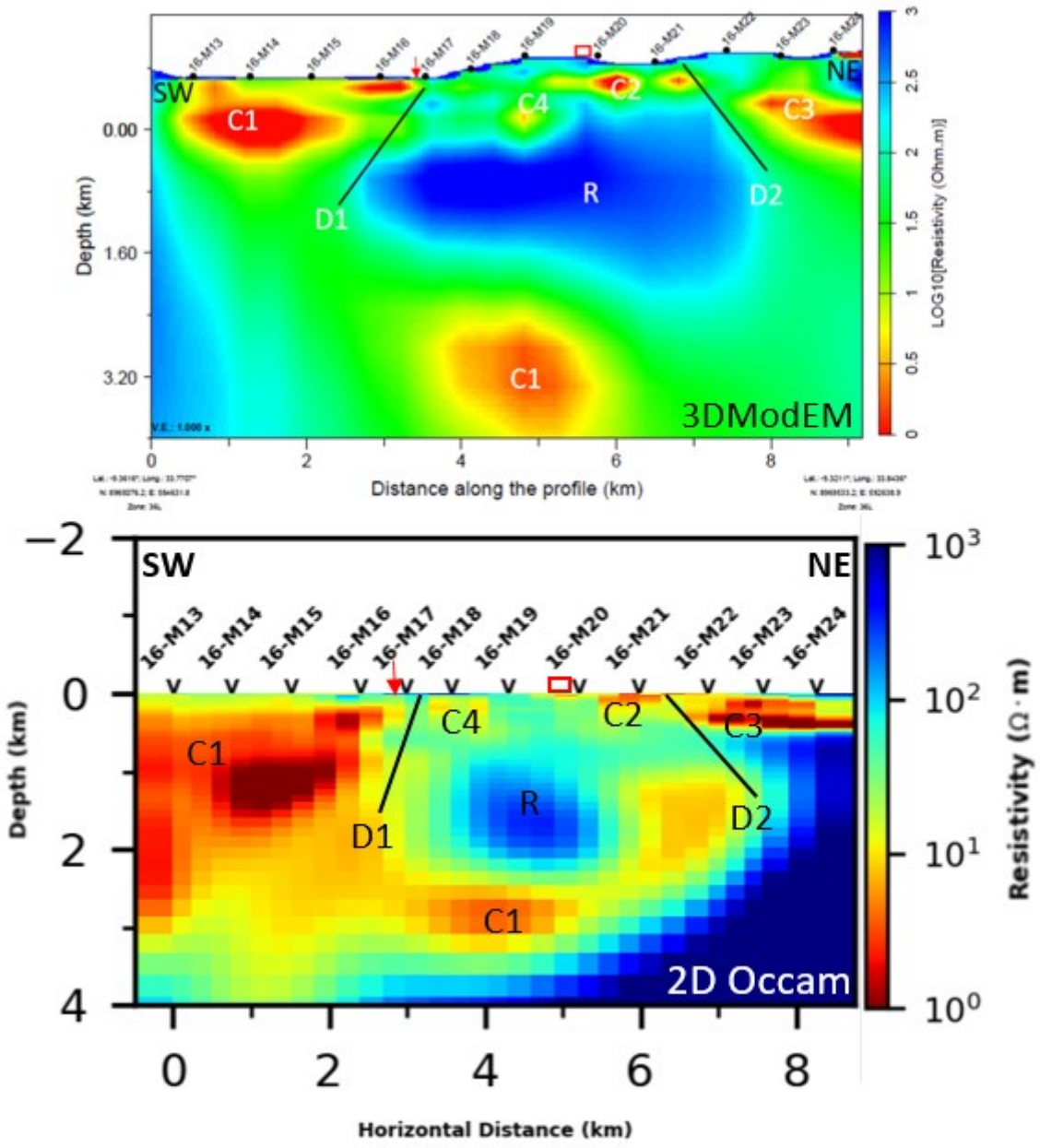

Figure 17: Continued; WSW-ENE trending profile line KML3. The Mbaka fault is marked by red arrow, while the Lufundo manifestation is indicated by red square.

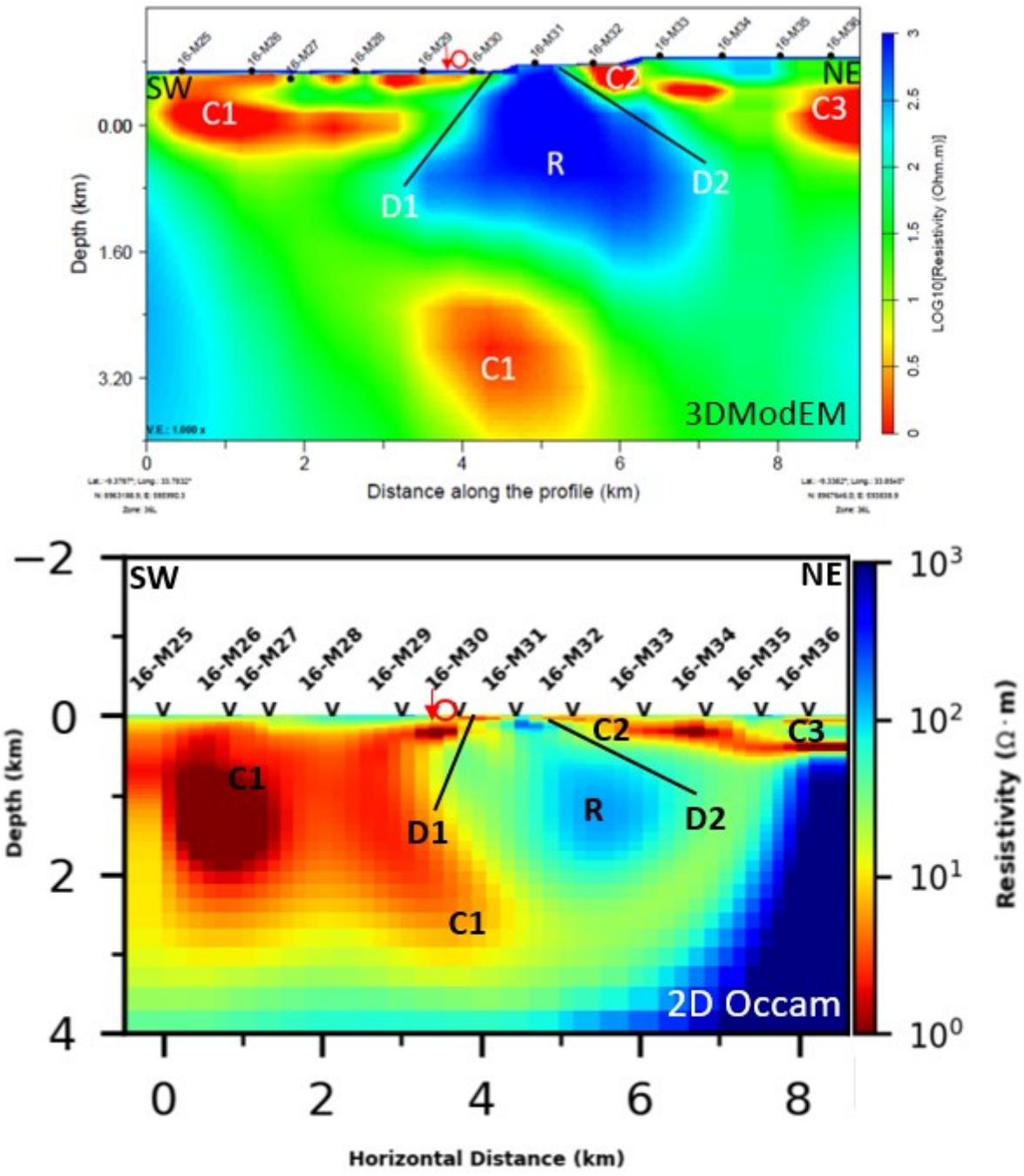

Figure 17: Continued; WSW-ENE trending profile line KML5. The Mbaka fault is marked by red arrow, while the Kilambo hot spring is indicated by red circle.

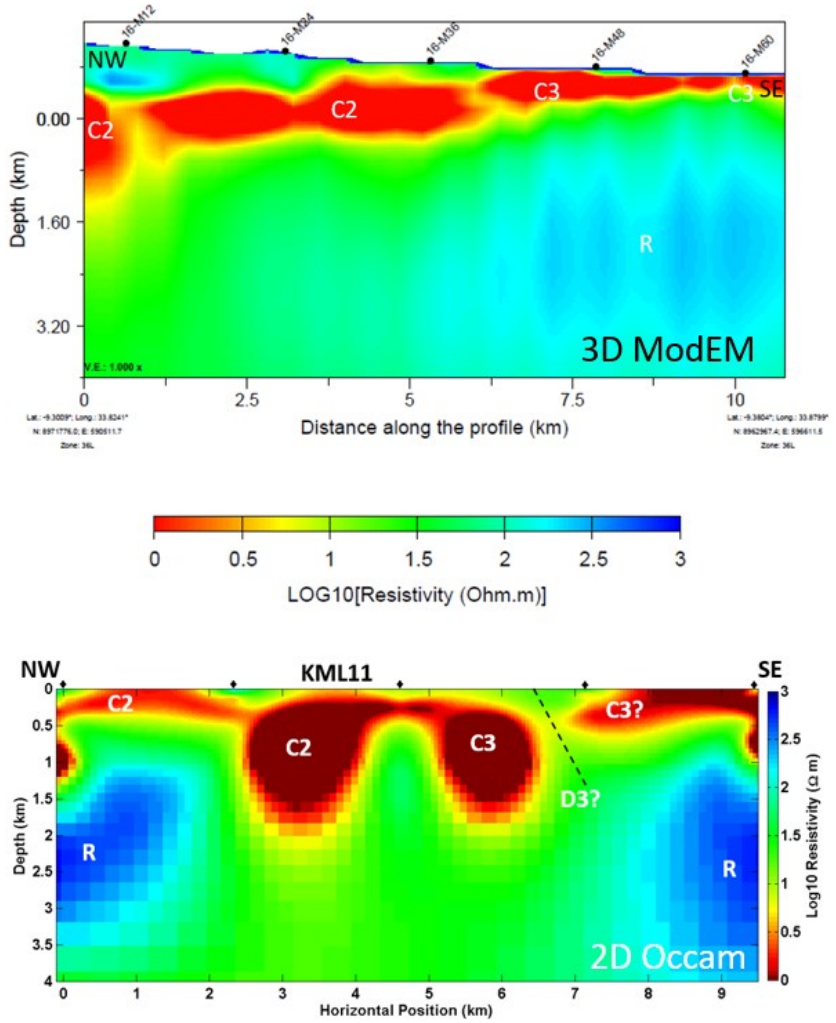

FIGURE 18: NNW-SSE trending profile line KML11.

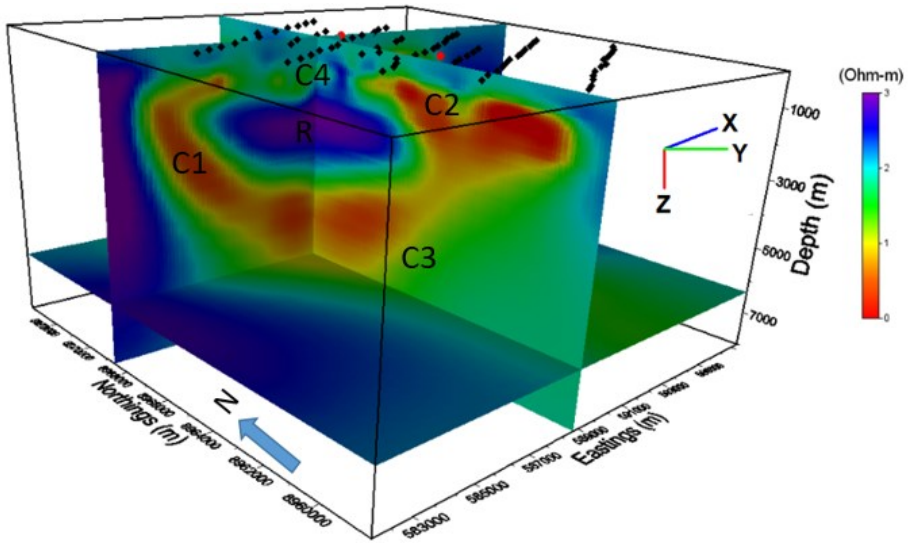

Figure 19: Two sections, E-W and N-S section, made from Voxel Software, to isolate the MIT central resistive body for comparisons with 3D-Grid-Academic tool and to test software artifacts. The sections speculating the order of resistivity from surface to deeper portion, Kilambo and Lufundo hot springs are marked by red dots for reference. MT sites are shown by black dots.

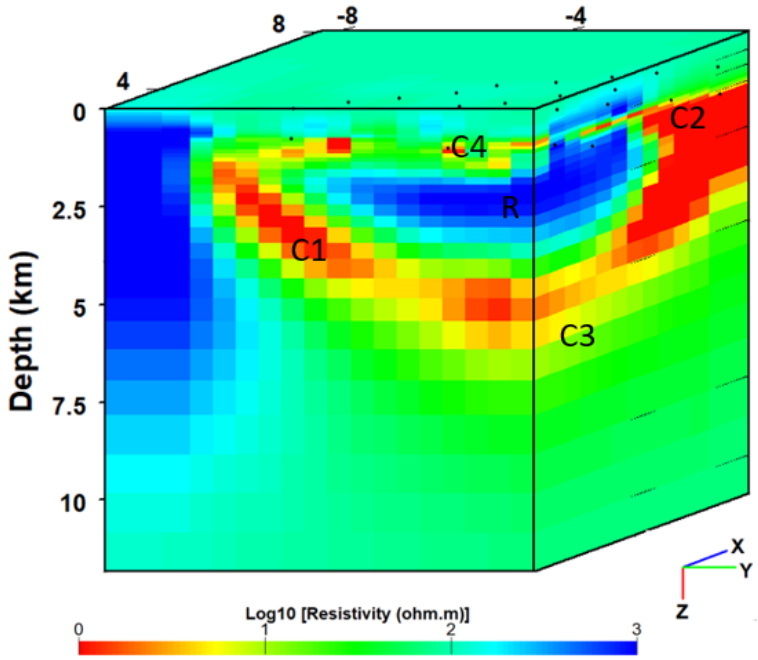

Figure 20: 3D resistivity model, made from 3D-Grid-Academic tool, to isolate the MIT central resistive body for comparisons with Voxel software and to test software artifacts.

5.4 Horizontal Resistivity Depth Slices

The resistivity depth slices are presented in Figure 21; the depth are intended positively downwards and starts from 2,000 m b.s.l. to 3,500 m b.s.l. with the focus to define the resistive central body, comprised by the outcropping Intrusive Metamorphic basement complex (MIT). At relatively shallow depth the (MIT) is partially detected, whereas, at a depth of about 2,000 m b.s.l. appears to be prominent, and at great depth about 3,500 m b.s.l., the (MIT) disappears. At relatively great depth, conductivity signatures become prominent, probably at this great depth, the rift basin that comprises the sedimentary sequences like fluvio-lacustrine Neogene sediments in the rift basin is detected beneath the (MIT).

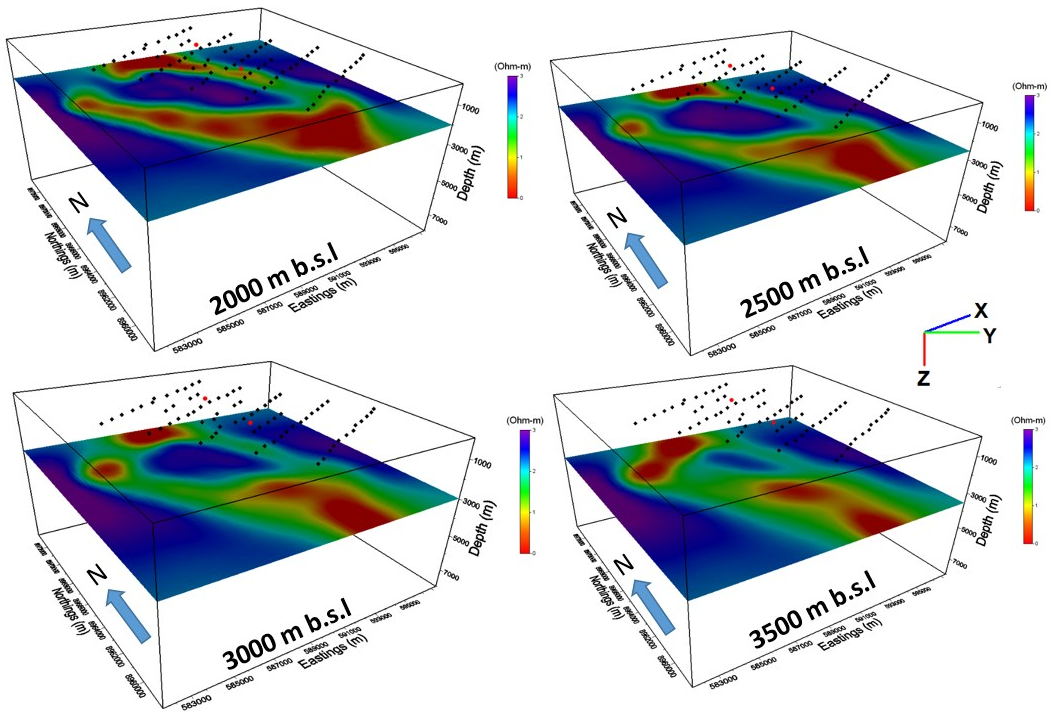

Figure 21: Resistivity depth slices from 2,000, 2,500, 3,000, and 3,500 m b.s.l. The MT sites are shown by black dots while the Kilambo and Lufundo hot spring are represented by red dots.

5.5 Temperature Alteration Synthesis Map

The main findings discussed in the previous section including the main features of the subsurface resistivity distributions recovered from 2-D and 3-D inversion results are superimposed on the geological map and temperature alteration zones mapped by ELC and TGDC (2016) modified and redrawn (Tumbu, 2019), we modified and replotted the geological map with some additional information to easy our interpretation. The recognized faults by ELC and TGDC (2016) are also reported. Moreover, notice that the showed features may not necessarily refer to the same depth.

The **AZ1**, **AZ2**, **AZ3** alteration zones shown in the Figure 22, have been inferred by considering the 10 Ωm iso-resistive contour line ELC and TGDC (2016) relevant to the resistivity anomalies discussed in previous sections (see 2-D and 3-D modelling). The **AZ4** zone Figure 22, has also been identified by considering the 50 Ωm contour line. Therefore, while the first three have to be referred as low-T alteration zones, the latter might be considered as a high-T one. Based on the available geological map, the assumption that all the alteration zones might have affected the metamorphic basement has to be considered ELC and TGDC (2016).

Zone **AZ1** corresponds to anomalies **C1**, given the SW-dipping of the Mbaka fault, could have affected not only the hanging wall but also the foot wall. In fact, the observation for trace of the Mbaka fault at surface, it can be easily assessed lying within zone **AZ1**.

Zone **AZ2** corresponds to the **C2** anomalies. This zone could be interpreted as a low-T alteration zone, possibly being related to the Lufundo manifestations.

Zone **AZ3** corresponds to **C3** anomalies. This zone could be interpreted as a low-T alteration zone, it has been only partially imaged by MT, and its eastern limit is still hypothetical.

Zone **AZ4** corresponds to the anomalies **C4** and could be correlated with the N-S fault passing about 1 km west of Lufundo, and it could represent a high-T alteration zone possibly associated with the Lufundo manifestations. (see 2-D and 3-D modelling).

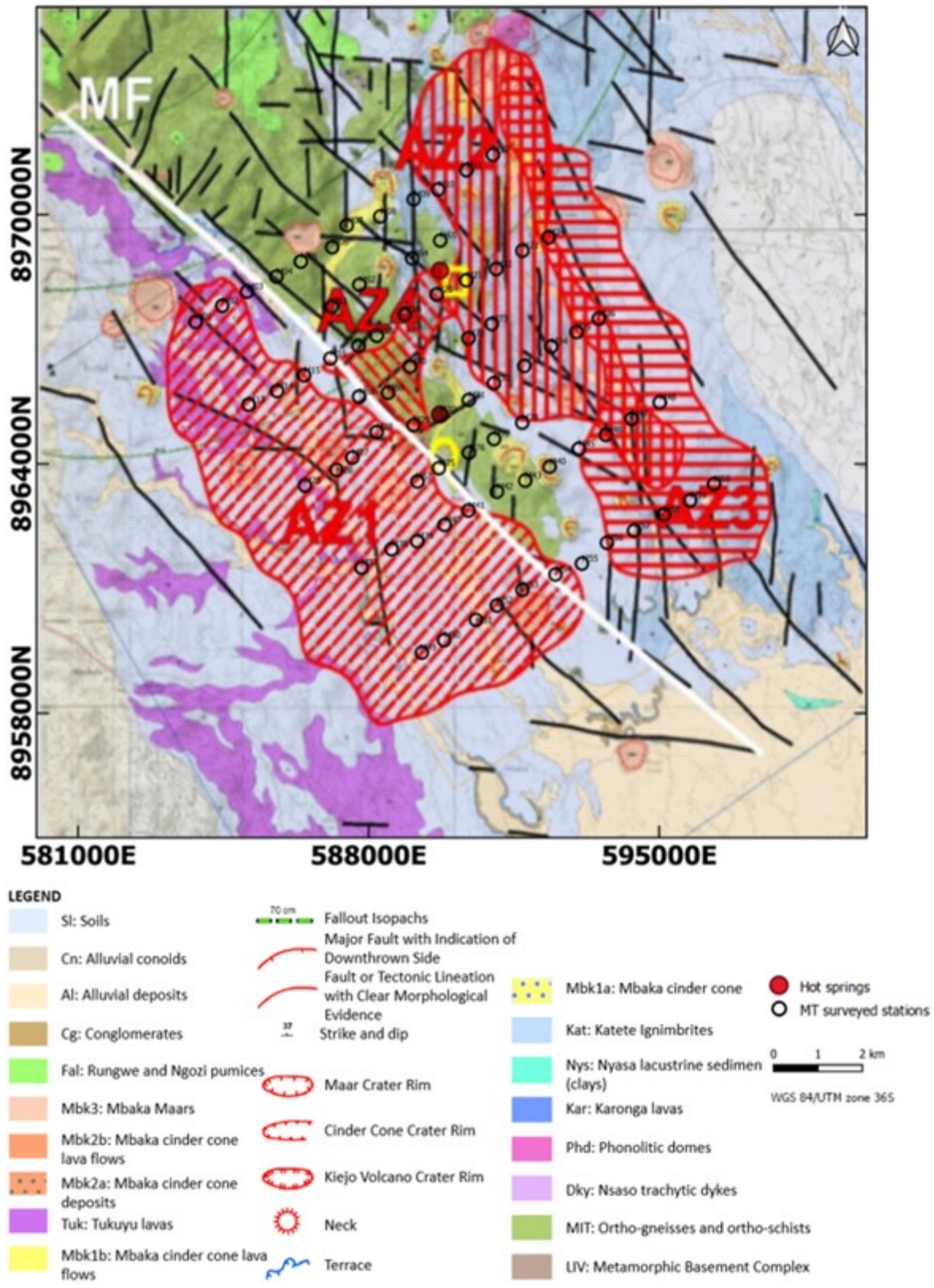

Figure 22: Synthesis map with the main findings superimposed on the geological map. Red dot: Kilambo and Lufundo hot springs. AZ1, AZ2, AZ3, AZ4: alteration zones, marked by different hatches. MF: Mbaka fault trace. Geological map ELC and TGDC (2016), modified and redrawn from (Tumbu, 2019).

6. CONCLUSIONS

2-D models beneath a few surveyed profile lines in Kiejo-Mbaka geothermal field, generated ambiguous structures at the boundary between the low resistivity and high resistivity from **MIT**. It implies a limitation of 2-D interpretation. On the other hand, the 3-D models seem to be more realistic for the entire resistivity models. Based on these experiences, it can be stated that, the 2-D inversion is often insufficient in geothermal exploration, particularly in a complicated geological environment, and that the 3-D interpretation is essential for geothermal exploration. If the measured data exhibit clear 3D effects like that of Kiejo-Mbaka study area, it is problematic to invert them with 2-D models, irrespective of whether two, three, or four degrees of freedom are used as input data.

The results of 2-D and 3-D inversions are similar, reconstructed the subsurface conductivity distributions of the study area, by recovering the subsurface structures and delineating the Mbaka fault from the Livingstone fault. The outcropping Intrusive Metamorphic basement complex (**MIT**), has excellently been detected as a resistive central body surrounded by four conductive anomalies, three of which are referred to low-T alteration zones and the fourth one being a high-T alteration zone.

The temperature alteration map, with its four alteration zones are in good agreement and correlate to the four main resistivity distributions reconstructed from 2-D and 3-D inversions results. The confidence that these structures are well-constrained by the data is elevated, in spite of the different setup and assumptions in the codes used, these structures are required, so they can be interpreted in terms of geology with more certainty.

REFERENCES

Biggs, J., Nissen, E., Craig, T., Jackson, J., & Robinson, D. P. (2010). Breaking up the hanging wall of a rift-border fault: The 2009 Karonga earthquakes, Malawi. *Geophysical Research Letters*, **37**, 1–5.

Constable, S. C., Parker, R. L., Constable, C. G., & Carlo, M. (1987). Occam's Invertion: A practical algorithm to generating smooth models from electromagnetic souding data, **52**.

deGroot-Hedlin, C., & Constable, S. (2002). Occam's inversion to generate smooth, two-dimensional models from magnetotelluric data. *Geophysics*, **55**, 1613–1624.

Delvaux, D. F., & Hanon, M. (1993). Neotectonics of the Mbeya Area, Sw Tanzania. *Mus. Roy. Afr. Centr.*, **97**, 87–97.

Ebinger, C. J., Deino, A. L., Tesha, A. L., Becker, T., & Ring, U. (1993). Tectonic controls on rift basin morphology: Evolution of the northern Malawi (Nyasa) Rift. *Journal of Geophysical* Jupp, D. L. B., & Vozoff, K. (1977). Two-dimensional magnetotelluric inversion. *Geophysical Journal of the Royal Astronomical Society*, **50**, 333–352.

Ledo, J. (2006). Erratum: 2-D versus 3-D magnetotelluric data interpretation. *Surveys in Geophysics*, **27**, 111–148.

Ledo, J., Queralt, P., Martí, A., & Jones, A. G. (2002). Two-dimensional interpretation of three-dimensional magnetotelluric data: An example of limitations and resolution. *Geophysical Journal International*, **150**, 127–139.

Muñoz, G. (2014). Exploring for Geothermal Resources with Electromagnetic Methods. *Surveys in Geophysics*, **35**, 101–122.

Ogawa Y. (2002). On two-dimensional modeling of magnetotelluric field data. *Surveys in Geophysics*, **23**, 251–272.

Siripunvaraporn, W., Egbert, G., & Uyeshima, M. (2005). Interpretation of two-dimensional magnetotelluric profile data with three-dimensional inversion: Synthetic examples. *Geophysical Journal International*, **160**, 804–814.

Uchida, T. (2005). Three-Dimensional Magnetotelluric Investigation in Geothermal Fields in Japan and Indonesia. *World Geothermal Congress 2005*, 24–29.

W., S., G., E., & Uyeshima M. (2005). Interpretation of two-dimensional magnetotelluric profile data with three-dimensional inversion: Synthetic examples. *Geophysical Journal International*, **160**, 804–814.